JOURNAL OF THERMOPHYSICS AND HEAT TRANSFER
Vol. 20, No. 4, October–December 2006

Improved Inverse Method for Radiative Characteristics of Closed-Cell Absorbing Porous Media

Jaona Randrianalisoa* and Dominique Baillis†
Centre de Thermique de Lyon, Institut National des Sciences Appliquées de Lyon, 69621 Villeurbanne Cedex, France
and
Laurent Pilon‡
University of California, Los Angeles, Los Angeles, California 90095-1597

DOI: 10.2514/1.16684

Radiative characteristics such as the extinction coefficient, the scattering albedo, and the scattering phase function of fused quartz containing closed cells are determined by using an inverse method based on theoretical and experimental bidirectional transmittances. The theoretical transmittances are obtained by solving the radiative transfer equation with the discrete ordinate method. Improvements have been made over previously reported experimental determination of porous fused quartz radiative characteristics by using a more accurate phase function and an adaptive quadrature to compute more precisely the intensities in the measurement directions. In addition, a two-step inverse method to compute accurately and simultaneously the radiative parameters has been developed. The results are shown to be independent of samples thickness. Exhaustive comparison between experimental measurements of hemispherical transmittance and reflectance and computational results using the retrieved radiative characteristics shows good agreement. The retrieved absorption coefficient of porous fused quartz appears to be more realistic than that reported in our earlier publication.

Nomenclature

a	=	bubble radius, m
b	=	corrective factor used in Eq. (10)
c_{ij}	=	matrix elements of the sensitivity coefficients J
e	=	sample thickness, m
f_1, f_2	=	spectral weights of the Henyey–Greenstein phase function Φ_{HG}
g	=	spectral asymmetry factor
g_1, g_2	=	spectral parameters of the Henyey–Greenstein phase function Φ_{HG}
I	=	spectral radiation intensity, $W \cdot m^{-2} \cdot sr^{-1}$
J	=	matrix of the sensitivity coefficients
k	=	volumetric absorption coefficient, m^{-1}
Mb	=	quadrature order of the discrete ordinate method
m	=	fused quartz refractive index
Nb	=	number of measurement directions
n	=	number of unknown parameters including ω, β, f_1, g_1, and/or g_2
p	=	unknown parameter such as ω, β, f_1, g_1, or g_2
Q	=	ratio of the measured scattered to the incident radiation fluxes
r	=	interface reflectivity
S	=	minimization function
T	=	spectral transmittance or reflectance, sr^{-1}
$\bar{T}$	=	average spectral transmittance or reflectance, sr^{-1}
w	=	angular weight of the discrete ordinate method
w'	=	angular weight of the two Gaussian quadratures associated to the experimental directions
x	=	bubble size parameter
y	=	spatial coordinate along the sample thickness, m
α	=	angle between incident radiation and measurement directions, rad
β	=	volumetric extinction coefficient, m^{-1}
γ	=	relaxation factor used in Eq. (5)
$\Delta\theta$	=	divergence angle of the incident radiation, rad
$\Delta\Omega$	=	solid angle, sr
δ	=	Kronecker delta function
$\varepsilon_0, \varepsilon_1, \varepsilon_2, \varepsilon_3$	=	coefficients of the third order polynomial estimating T_{sca} in Eq. (17)
η	=	cosine of the angle α
Θ	=	scattering angle defined in Eq. (21), rad
θ	=	angle between incident radiation direction and radiation inside the porous medium, rad
κ	=	fused quartz absorption index
λ	=	radiation wavelength, m
μ	=	cosine of the angle θ
ν_i	=	weight associated to measurement in the direction $i = 1$ to Nb
ξ	=	random number defined between 0 and 1
Π	=	dimensionless sensitivity coefficient
σ	=	standard deviation
τ_0	=	optical thickness
Φ	=	spectral phase function
φ	=	azimuthal angle, rad
χ	=	experimental error, %
ω	=	volumetric scattering albedo

Superscripts

$+$	=	refers to hemispherical transmittance
$-$	=	refers to hemispherical reflectance

Subscripts

bulk	=	refers to the continuous phase (quartz)
coll	=	refers to collimated radiation

Received 17 March 2005; revision received 26 October 2005; accepted for publication 26 October 2005. Copyright © 2005 by the American Institute of Aeronautics and Astronautics, Inc. All rights reserved. Copies of this paper may be made for personal or internal use, on condition that the copier pay the $10.00 per-copy fee to the Copyright Clearance Center, Inc., 222 Rosewood Drive, Danvers, MA 01923; include the code $10.00 in correspondence with the CCC.

*Ph.D. Student, CETHIL UMR CNRS 5008, Domaine Scientifique de la Doua, INSA de Lyon, Bâtiment Sadi Carnot, 9 rue de la Physique; jaona.randrianalisoa@insa-lyon.fr.

†Assistant Professor, CETHIL UMR CNRS 5008, Domaine Scientifique de la Doua, INSA de Lyon, Bâtiment Sadi Carnot, 9 rue de la Physique; dominique.baillis@insa-lyon.fr.

‡Assistant Professor, Mechanical and Aerospace Engineering Department, 37-132 Engineering IV, Box 951597; pilon@seas.ucla.edu.

d	=	refers to detection
e	=	refers to experimentally measured value
exact	=	refers to the exact radiative parameters
HG	=	Henyey–Greenstein phase function
max, min	=	refers to the higher and lower integration bound in Eq. (30), respectively
NC	=	refers to the Nicolau phase function
sca	=	refers to the scattered
t	=	refers to the theoretical value
TPF	=	refers to the truncated phase function
λ	=	refers to spectral value
0	=	refers to incident radiation
12	=	refers to radiation from the air to the air-glass interface
21	=	refers to radiation from the glass to the glass-air interface

I. Introduction

FOAM and cellular materials have practical importance in many applications. Examples range from food processes, where foam can disrupt the process, to space and building applications where they are used as insulating materials. Thermal radiation in cellular materials is a significant mode of energy transfer in most of these applications. Thus, the modeling of radiative transfer in cellular materials is of primary importance for optimizing performance in engineering applications. An extensive review of radiative transfer in dispersed media was carried out by Viskanta and Mengüç [1] and by Baillis and Sacadura [2]. A porous medium is often treated as a continuous, homogeneous, absorbing, and scattering medium. To evaluate the radiative heat transfer, radiative characteristics such as the extinction coefficient, the scattering albedo, and the scattering phase function are required. They can be determined by different approaches:

1) Radiative characteristics can be predicted from porosity and bubble size distribution by considering a random arrangement of particles and by using, for example, the Mie theory or the geometric optics laws assuming independent scattering [3–8].

2) Other methods consist of determining the radiative characteristics from a Monte Carlo approach at the microscopic scale, taking into account the complex morphology of the porous medium [9–14].

3) Finally, other approaches are based on the experimental measurement of reflectance and transmittance of the medium on a macroscopic scale combined with an inverse method [15–20]. Hemispherical emittance measurements have also been exploited to retrieve the radiative characteristics of porous media [21,22].

The present study focuses on radiative characteristics of fused quartz containing bubbles or closed cells as illustrated in Fig. 1. Few studies on such media have been reported. Pilon and Viskanta [6] have studied the effects of volumetric void fraction and bubble size distribution on the radiative characteristics of semitransparent media containing gas bubbles. They used the model proposed by Fedorov and Viskanta [7], which is based on the anomalous-diffraction approximation. Wong and Mengüç [12] used a ray-tracing method in a porous medium composed of spherical air pockets embedded in a nonabsorbing matrix to study the depolarization of the incident radiation. More recently, experimental determination of radiative characteristics of fused quartz containing bubbles [18] based on an inverse method has been carried out. The Henyey–Greenstein phase function model was adopted and theoretical transmittance in the experimental directions was interpolated from the solution of the radiative transfer equation (RTE). The retrieved absorption coefficient of the porous fused quartz was found to be greater than that of dense fused quartz which, a priori, seems to contradict physical intuition because bubbles entrapped in the glass matrix are transparent [23,24]. On the other hand, the larger absorption coefficient could be attributed to trapping of radiation by successive interreflections within the bubbles [18] or to the increased optical path within the glass matrix due to reflections at the surface of the bubbles. These apparent contradictions are due to the choice of the phase function model used in the calculations of the theoretical bidirectional transmittance and reflectance and will be clarified in this paper.

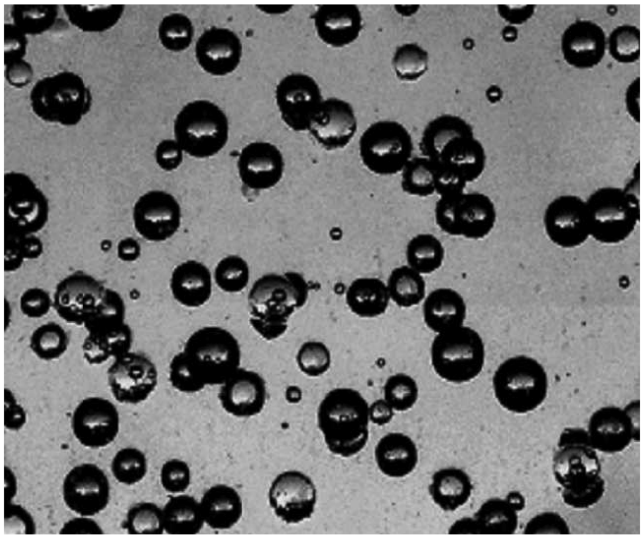

Fig. 1 Photo of the studied samples.

The present study aims at completing the previous one [18] by investigating 1) the influences of the phase function model on the retrieved radiative characteristics, 2) the best way to calculate the transmitted intensity in the specific measurement directions, and 3) the development of a more efficient identification technique. First, the inverse method using experimental and theoretical transmittances is described, including details regarding 1) different forms of the minimization and 2) different models of scattering phase functions, as well as 3) the direct computation of the extinction coefficient. Then, the experimental setup and the measurements are briefly presented whereas the theoretical model for calculating the bidirectional transmittance and reflectance is explained in detail. Finally, the results are presented and discussed.

II. Parameter Identification Method

A. Description

The spectral radiative characteristics of semitransparent media are the single scattering albedo ω_λ, the extinction coefficient β_λ, and the scattering phase function Φ_λ, which depends on n-2 parameters that will be here denoted by $(p_l)_{l=3,n}$. As a result, the n unknown parameters are $(p_l)_{l=1,\ldots,n} = (\omega, \beta, p_{l=3,n})$. For a given sample, the parameter identification method is based on 1) the experimental measurements of the bidirectional reflectance and transmittance (T_e) obtained for several directions (i) and 2) the theoretical bidirectional reflectance and transmittance (T_t) calculated for the same directions.

For each wavelength λ, the goal is to determine the radiative parameters $(p_l)_{l=1,\ldots,n}$, which minimize a function S characterized by the quadratic differences between the experimentally measured bidirectional transmittances $T_{e,i}$ and the corresponding numerically calculated value $T_{t,i}$ for Nb measurement directions:

$$S(p_1, \ldots, p_n) = \sum_{i=1}^{\mathrm{Nb}} \nu_i^2 [T_{ti}(p_1, \ldots, p_n) - T_{ei}]^2 \qquad (1)$$

The bidirectional transmittance or reflectance T_i for normal incident intensity are defined by the following expression:

$$T_i = \frac{I_i}{I_0 \Delta\Omega_0} \qquad (2)$$

where I_i is the transmitted or reflected intensity in the direction i and I_0 is the intensity of the collimated beam normally incident on the sample within the incident solid angle $\Delta\Omega_0$. The weight ν_i, associated with the direction i, is introduced to decrease the importance of inaccurate measurements.

The optimization method adopted is the Gauss linearization method [25], which minimizes S by setting to zero the derivatives of Eq. (1) with respect to each of the unknown parameters. As the system is nonlinear, an iterative procedure is performed over j iterations:

$$\begin{bmatrix} \sum_{i=1}^{\mathrm{Nb}} \nu_i^2 \left(\frac{\partial T_{ti}}{\partial p_1}\right)^2 & \sum_{i=1}^{\mathrm{Nb}} \nu_i^2 \left(\frac{\partial T_{ti}}{\partial p_1}\right)\left(\frac{\partial T_{ti}}{\partial p_2}\right) & \cdots & \sum_{i=1}^{\mathrm{Nb}} \nu_i^2 \left(\frac{\partial T_{ti}}{\partial p_1}\right)\left(\frac{\partial T_{ti}}{\partial p_n}\right) \\ \sum_{i=1}^{\mathrm{Nb}} \nu_i^2 \left(\frac{\partial T_{ti}}{\partial p_1}\right)\left(\frac{\partial T_{ti}}{\partial p_2}\right) & \sum_{i=1}^{\mathrm{Nb}} \nu_i^2 \left(\frac{\partial T_{ti}}{\partial p_2}\right)^2 & \cdots & \sum_{i=1}^{\mathrm{Nb}} \nu_i^2 \left(\frac{\partial T_{ti}}{\partial p_2}\right)\left(\frac{\partial T_{ti}}{\partial p_n}\right) \\ \cdots & \cdots & \cdots & \cdots \\ \sum_{i=1}^{\mathrm{Nb}} \nu_i^2 \left(\frac{\partial T_{ti}}{\partial p_1}\right)\left(\frac{\partial T_{ti}}{\partial p_n}\right) & \sum_{i=1}^{\mathrm{Nb}} \nu_i^2 \left(\frac{\partial T_{ti}}{\partial p_1}\right)\left(\frac{\partial T_{ti}}{\partial p_n}\right) & \cdots & \sum_{i=1}^{\mathrm{Nb}} \nu_i^2 \left(\frac{\partial T_{ti}}{\partial p_n}\right)^2 \end{bmatrix}^j \begin{bmatrix} \Delta p_1 \\ \Delta p_2 \\ \cdots \\ \Delta p_n \end{bmatrix}^j = \begin{bmatrix} \sum_{i=1}^{\mathrm{Nb}} \nu_i^2 (T_{ti} - T_{ei}) \frac{\partial T_{ti}}{\partial p_1} \\ \sum_{i=1}^{\mathrm{Nb}} \nu_i^2 (T_{ti} - T_{ei}) \frac{\partial T_{ti}}{\partial p_2} \\ \cdots \\ \sum_{i=1}^{\mathrm{Nb}} \nu_i^2 (T_{ti} - T_{ei}) \frac{\partial T_{ti}}{\partial p_n} \end{bmatrix}^j \tag{3}$$

The solution of the system of Eq. (3) gives the variation parameter Δp_l^j added to the value of each parameter p_l^j at the jth iteration, i.e.,

$$p_l^{j+1} = p_l^j + \Delta p_l^j \quad \text{with } l = 1, 2, \ldots, n \tag{4}$$

The use of Eq. (4) limits the convergence of the inverse process due to large values of Δp_l^j during the first few iterations. In this study, we propose to weight the parameter Δp_l^j with a relaxation factor $\gamma (1 \geq \gamma > 0)$:

$$p_l^{j+1} = p_l^j + \gamma \Delta p_l^j \quad \text{with } l = 1, 2, \ldots, n \tag{5}$$

The converged solution is estimated to be reached when $\Delta p_l^j / p_l^j < 10^{-3}$. The matrix on the left-hand side of Eq. (3) will be termed J. It is composed of the sensitivity coefficients $\partial T_{ti} / \partial p_l$ calculated from the theoretical model. The condition number (CN) of the matrix J can be calculated from the following relation:

$$\mathrm{CN}(J) = \|J^{-1}\| \cdot \|J\| \tag{6}$$

where $\|J\|$ is the norm of the matrix, calculated from the matrix elements c_{ij} as follows:

$$\|J\| = \max_{i=1,n} \sum_{j=1}^{n} c_{ij} \tag{7}$$

Note that the condition number is always larger than unity. The larger CN is, the more ill-conditioned the system. Thus, small uncertainties in the measurements can result in very large changes in the Δp vector. A large condition number occurs when at least two of the sensitivity coefficients are quasilinearly interdependent and/or when at least one is very small or very large compared with the others. The analysis of the sensitivity coefficients and the condition number is an efficient tool for understanding the physical behavior of the problem and for studying the feasibility of simultaneous determination of the unknown parameters [26].

B. Measurements Weights

Two common expressions for the weights can be used [17–19]:

$$\nu_i = 1 \quad \text{for } i = 1 \text{ to Nb} \tag{8}$$

$$\nu_i = \frac{1}{T_{ei}} \quad \text{for } i = 1 \text{ to Nb} \tag{9}$$

When using Eq. (8), the minimization gives more importance to the highest measurement values. This is inconvenient in the situation where physical information is "hidden" behind small values of transmittances. Instead, using Eq. (9) enables one to give the same importance to each measurement and appears to be more appropriate.

Usually, some measurements feature large experimental uncertainties as detailed hereafter in Section III.B. Such data can potentially contain information about the porous material. It is therefore preferable to decrease the importance of that data in the identification procedure rather than to discard them completely. This can be done by modifying the weight ν_i by a corrective factor b_i as follows [20]:

$$\nu_i = \frac{b_i}{T_{ei}} \quad \text{for } i = 1 \text{ to Nb} \tag{10}$$

The value of the parameter b_i depends on the accuracy of the measurements estimated through the experimental errors χ discussed in Section V.C. In this study, the following values were used for different measurement error ranges:

$$\begin{cases} \chi_i < 10\% & \Rightarrow b_i = 1 \\ 10\% < \chi_i < 20\% & \Rightarrow b_i = 0.1 \\ \chi_i > 20\% & \Rightarrow b_i = 0.01 \end{cases} \quad \text{for } i = 1 \text{ to Nb} \tag{11}$$

The weights given by Eqs. (10) and (11) for different experimental uncertainties are adopted in this study.

C. Models for the Scattering Phase Function

The expression for the phase function plays an important role in describing the appropriate directional scattering behavior. In practice, the representation of the scattering phase function as an expansion in Legendre polynomial [27] is not suitable in the case of highly anisotropic material due to the larger number of unknown parameters [20]. Among the useful models, the Henyey–Greenstein approximation [28] is the most popular with only one unknown parameter g_λ:

$$\Phi_{\mathrm{HG}}(\Theta, g_\lambda) = \frac{1 - g_\lambda^2}{(1 + g_\lambda^2 - 2 g_\lambda \cos\Theta)^{3/2}} \tag{12}$$

where Θ is the angle between the directions of the incident and scattered radiation intensities at a scattering point.

However, some materials having a more complex anisotropic scattering pattern require the use of a more complex scattering function to properly describe the directional scattering behavior. For example, Nicolau et al. [19] proposed a combination of Heyney–Greenstein functions for fibrous media:

$$\Phi_{\mathrm{NC}}(\Theta, g_{1\lambda}, g_{2\lambda}, f_{1\lambda}, f_{2\lambda}) = f_{2\lambda}[f_{1\lambda}\Phi_{\mathrm{HG}}(\Theta, g_{1\lambda}) + (1 - f_{1\lambda})\Phi_{\mathrm{HG}}(\Theta, g_{2\lambda})] + (1 - f_{2\lambda}) \tag{13}$$

where $f_{1\lambda}$ and $f_{2\lambda}$ are the weights associated to the scattering functions $\Phi_{\mathrm{HG}}(\Theta, g_{1\lambda})$ and $[f_{1\lambda}\Phi_{\mathrm{HG}}(\Theta, g_{1\lambda}) + (1 - f_{1\lambda})\Phi_{\mathrm{HG}}(\Theta, g_{2\lambda})]$, respectively.

According to the previous study [19], the simultaneous computation of these parameters combined with the extinction coefficient and the scattering albedo remains critical. The reduction of the number of unknown parameters (ω, β, f_1, f_2, g_1, and g_2) to be simultaneously identified is required.

This study proposes a new combination of scattering functions called the truncated phase function (TPF) depending only on three parameters (f_1, g_1, and g_2):

$$\begin{cases} \Phi_\lambda(\Theta, f_1, g_1, g_2) = \Phi_{1\lambda}(\Theta, f_1, g_1, g_2) = f_1\Phi_{HG\lambda}(\Theta, g_1) + (1-f_1)\Phi_{HG\lambda}(\Theta, g_2) & \text{for } 0 \le \Theta \le \pi/2 \\ \Phi_\lambda(\Theta, f_1, g_1, g_2) = 0.03\Phi_{1\lambda}(\Theta, f_1, g_1, g_2) & \text{elsewhere} \end{cases} \tag{14}$$

Figure 2 compares the TPF to the exact Mie scattering phase function [29] in the case of an optically large bubble ($x = 2\pi a/\lambda = 2000$) located in a refracting medium ($m_\lambda = 1.44$). The corresponding TPF parameters are $f_1 = 0.2$, $g_1 = 0.98$, and $g_2 = 0.45$. One can note that the TPF function can properly approximate the exact phase function.

The method previously adopted by Nicolau et al. [19] is used to normalize this function. The resulting function satisfies

$$\frac{1}{2}\int_0^\pi \Phi_\lambda(\Theta, f_1, g_1, g_2)\sin\Theta\, d\Theta = 1 \tag{15}$$

The asymmetry factor corresponding to this phase function is given by [29]

$$g_\lambda = \frac{1}{2}\int_0^\pi \Phi_\lambda(\Theta, f_1, g_1, g_2)\cos\Theta\sin d\Theta \tag{16}$$

D. Direct Estimation of the Extinction Coefficient

The collimated transmittance T_{coll} in the incident radiation direction which is attenuated only by extinction and reflection at interfaces can be written as [28]

$$T_{coll} = T_{e1} - T_{sca1} = \frac{(1-r_{12})^2\exp(-\beta e)}{1-r_{12}^2\exp(-2\beta e)} \tag{17}$$

where T_{e1} refers to the measured transmittance in the incident direction whereas T_{sca1} refers to the scattered transmittance toward the same direction. The subscript 1 refers to the first direction of measurement ($i = 1$) which is, in this study, the same as the incident radiation direction. The Fresnel reflectivity is denoted r_{12} at the air-glass interface for normal incidence and e is the sample thickness.

Here, T_{sca1} is estimated by a third order polynomial in terms of the measurement direction cosine $\eta(=\cos\alpha)$, i.e., $T_{scai} = \varepsilon_3\eta_i^3 + \varepsilon_2\eta_i^2 + \varepsilon_1\eta_i + \varepsilon_0$ with $i = 1$ and $\eta_1 = 1$. The four coefficients ε_0, ε_1, ε_2, and ε_3 are obtained by matching the conditions $T_{scai} = T_{ei}$ for the four directions $i = 2$–5.

After some manipulations of Eq. (17), the extinction coefficient can be expressed as

$$\beta = -\frac{1}{e}\ell n\left(\frac{\sqrt{(1-r_{12})^4 + 4T_{coll}^2 r_{12}^2} - (1-r_{12})^2}{2T_{coll}r_{12}^2}\right) \tag{18}$$

The extinction coefficient can be directly calculated from Eq. (18). Thus, the set of unknown parameters to be simultaneously identified is reduced to ω, f_1, g_1, and g_2.

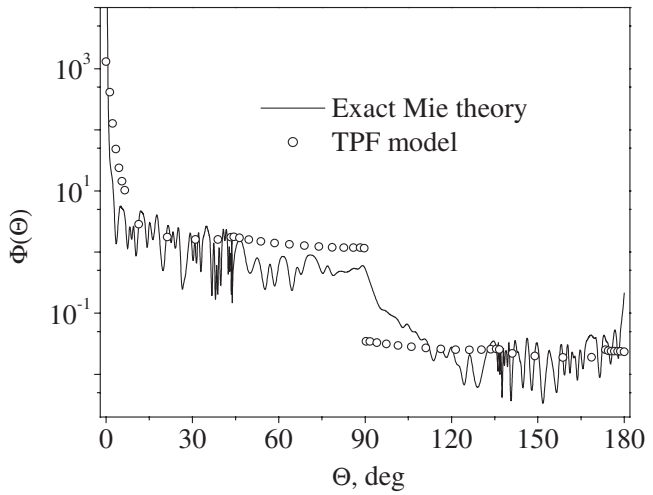

Fig. 2 Mie scattering function of an optically large bubble of size parameter $x = 2000$ and TPF function characterized by $f_1 = 0.2$, $g_1 = 0.98$, and $g_2 = 0.45$.

III. Experimental Measurements

A. Experimental Setup

The experimental data of spectral bidirectional transmittance and reflectance are obtained from an experimental setup including a Fourier–Transform infrared spectrometer (FTS 60 A, Bio-Rad Inc.) associated with a detector (liquid nitrogen cooled MCT detector) mounted on a goniometric system [17–19]. The incident radiation emitted by the source is modulated after which the resulting spectrum range varies from 1.67 to 14 μm. The collimated beam is perpendicularly incident on the sample with a divergence half-angle of $\Delta\theta_0 = 2.21\ 10^{-2}$ rad and a beam size d equal to 40 mm. We assume that the samples are thin enough (see Section V.A) to guarantee one-dimensional radiation transfer. Unfortunately, to the best of our knowledge, no criteria for the ratio of sample thickness to beam diameter is available in the literature. Note that measurements were performed with and without a gold coating deposited on the edges of the slab. No noticeable effects were recorded indicating that the side boundary conditions have no effect on the directional transmittance and reflectance. Therefore, the problem can be treated as one-dimensional.

The intensity transmitted or reflected by the sample is collected by a spherical mirror which focuses it on the detector. The corresponding detection solid angle ($\Delta\Omega_d$) is characterized by a detection half-angle equal to $\Delta\theta_d = 0.33\ 10^{-2}$ rad.

Then, the measured bidirectional transmittance in the direction i can be computed from [30]

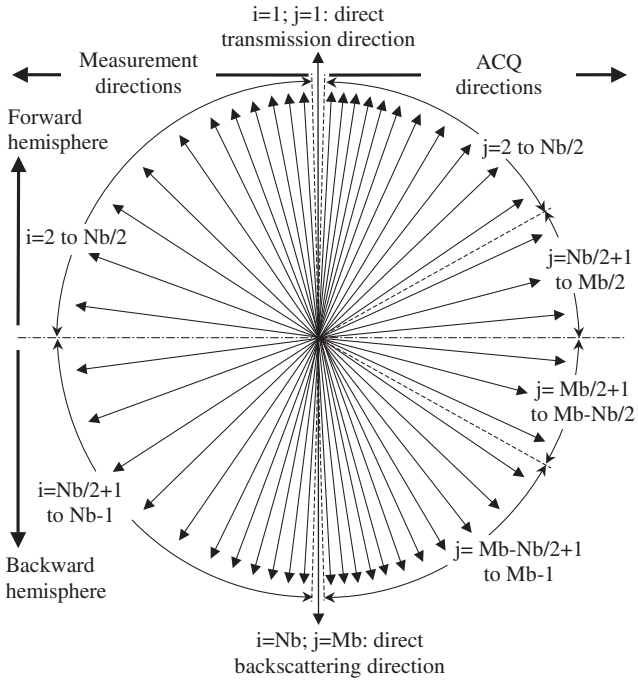

Fig. 3 Measurement and ACQ directions.

$$T_{ei} = \frac{I(\eta_i)}{I_0 \Delta\Omega_0} = \frac{Q_i}{\eta_i \max(\Delta\Omega_d, \Delta\Omega_0)} \tag{19}$$

where Q_i is the ratio of the radiation flux transmitted or reflected by the sample to that incident on the sample, directly estimated from the FTIR measurement in the direction i. The incident and detection solid angles can be expressed as $\Delta\Omega_0 = 2\pi(1 - \cos\Delta\theta_0)$ and $\Delta\Omega_d = 2\pi(1 - \cos\Delta\theta_d)$, respectively [30].

The bidirectional measurements are carried out over $\mathrm{Nb} = 24$ directions as shown in Fig. 3: 12 directions in the forward hemisphere (transmittances) and 12 directions in the backward hemisphere (reflectances). These directions are chosen by combining two Gaussian quadratures aimed at increasing the number of measurements around the direction of the incident radiation and suitable for forward and/or backward scattering media [19]. Note that Nb must be a positive even number and is maintained equal to 24 in this study.

B. Measurement Uncertainties

There are two major sources of experimental uncertainties involved in the bidirectional FTIR measurements, namely noise and misalignment. Indeed, the measurements become erroneous when the signal to noise ratio is too small. It is the case for our measurements 1) at wavelengths beyond 4.04 μm for which the fused quartz becomes optically thick and 2) far from the incident radiation direction (from 48 to 90 deg for transmittances and from 90 to 148 deg for reflectances) where the magnitude of the scattered radiative flux is small.

Moreover, for the measurement in the second direction (the closest to the incident radiation direction), the signal decreases sharply and a slight overestimation of the measured signal occurs due to the diffraction of the incident beam from the aperture inside the FTIR spectrometer. Also, the same problem occurs for measurement close to the backward specular direction (i.e., the direction Nb-1). Measuring precisely the specular reflectance is also difficult with our goniometric system due to the optical misalignments.

To reduce these uncertainties, the measurements are repeated five times (each one corresponding to a new goniometric system alignment) and the resulting average bidirectional transmittances and reflectances are used in the inversion procedure. Moreover, only the essential measurements which are required for identification are retained. These measurements are presented and analyzed in Sections V.B and V.C.

IV. Theoretical Model

The theoretical spectral bidirectional transmittance and reflectance are computed by solving the radiative transfer equation based on the assumptions that 1) radiative transfer is one-dimensional, 2) a steady-state regime is established, 3) azimuthal symmetry prevails, and 4) medium emission can be disregarded thanks to the radiation modulation and the phase sensitive detection.

A. RTE and Boundary Conditions

Under the preceding assumptions, the RTE can be written as follows [18]:

$$\mu \frac{\partial I_\lambda(y,\mu)}{\beta_\lambda \partial y} + I_\lambda(y,\mu) = \frac{\omega_\lambda}{2} \int_{-1}^{1} I_\lambda(y,\mu') \Phi_\lambda(\Theta)\, \mathrm{d}\mu' \tag{20}$$

where y indicates the spatial coordinate along the sample thickness and μ is the direction cosine of the intensity with respect to the y-axis.

The scattering angle Θ can be expressed in terms of the direction cosines μ and μ' as [31]

$$\Theta = \cos^{-1}\{\mu\mu' + [(1-\mu^2)(1-\mu'^2)]^{1/2} \cos\varphi\} \tag{21}$$

where φ is the azimuthal angle which can take any arbitrary value in case of azimuthal symmetry [31].

The boundary conditions are obtained by assuming that the interfaces are optically smooth, i.e., the surface roughness is much smaller than the wavelength of the incident radiation and the area associated with the open bubbles at the sample surfaces is negligible due to the small void fraction. In fact, the sample surfaces are mechanically polished as described in the previous work [18] and the open bubbles occupy only 7.5% of the total sample surface exposed to the incident radiation. Then, the boundary conditions associated with the RTE for normal incident radiation are [18]

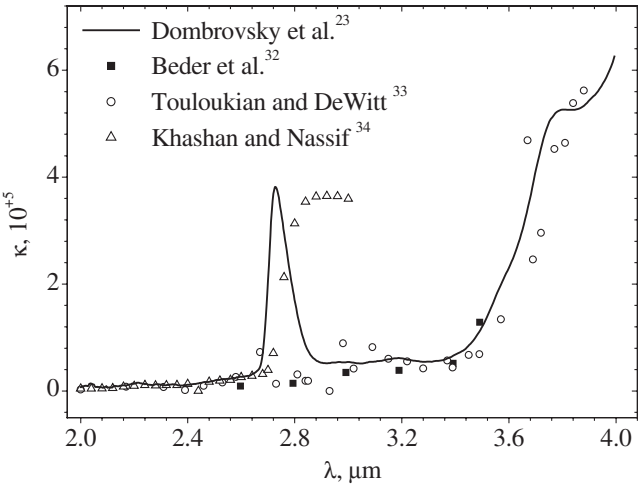

Fig. 4 Index of absorption of fused quartz from literature.

$$I_\lambda(0,\mu) = r_{21} I_\lambda(0,-\mu) + m_\lambda^2 (1 - r_{12}) \delta_{\mu_0,\mu} I_\lambda(0,\mu_0) \qquad \mu > 0 \tag{22}$$

$$I_\lambda(e,\mu) = r_{21} I_\lambda(e,-\mu) \qquad \mu < 0 \tag{23}$$

where r_{12} and r_{21} are the interfacial reflectivities at the air-glass and glass-air interfaces, respectively. The Kronecker delta function is defined as $\delta_{\mu_0,\mu} = 1$, if $\mu = \mu_0$ and $\delta_{\mu_0,\mu} = 0$, otherwise where $\mu_0 = 1$ in the case of normal incident radiation.

When the absorption index κ_λ is small, such as $\kappa_\lambda < 10^{-3}$, which is the case for fused quartz in the spectral range of interest from 1.67 to 4.04 μm as one can see in Fig. 4 , the reflectivities r_{12} and r_{21} are determined entirely from the refractive index m_λ by means of Fresnel's equations [28,31]. The air-glass reflectivity r_{12} for normal incident radiation can be calculated as [31]

$$r_{12} = \frac{(m_\lambda - 1)^2}{(m_\lambda + 1)^2} \tag{24}$$

Because of scattering by bubbles embedded in the continuous phase, the radiation field inside the porous slab does not reach the back face of the slab perpendicularly. Thus, the glass-air reflectivity r_{21} is given by [31]

$$r_{21} = \frac{1}{2}\left(\frac{\sin^2(\theta-\alpha)}{\sin^2(\theta+\alpha)} + \frac{\mathrm{tg}^2(\theta-\alpha)}{\mathrm{tg}^2(\theta+\alpha)}\right) \tag{25}$$

where $\theta = \cos^{-1}\mu$ is the angle between the internal radiation towards the surface of the slab and the y-axis, and $\alpha = \cos^{-1}\eta$ is the angle between the refracted radiation leaving the slab and the unit normal to the interface. The angles θ and α are related by Snell's law [31] expressed as

$$m_\lambda \sin\theta = \sin\alpha \tag{26}$$

B. Method of Solution of the RTE

The discrete ordinate method (DOM) [28,31,35] is applied to solve the RTE [Eq. (20)]. It consists of replacing the integral term in the RTE by a sum over Mb directions, constituting a "quadrature." Several standard quadratures such as the Gaussian, Radau, and Fiveland quadratures [36] can be used in the integral calculation. Then, a system of partial differential equations is obtained.

Previously reported studies on the experimental determination of radiative characteristics of open-cell porous media [17,19] neglected the reflection at the interfaces due to the large porosity of the medium. Then, a simpler system of equations could be solved analytically by separating the collimated and scattered radiation. In the present study, however, the system is more complicated due to the reflections at the front and back interfaces. Thus, the space is discretized along the y-direction to solve numerically the system of partial differential equations with the associated boundary conditions [Eqs. (22) and (23)] by using the control volume method [35]. A linear scheme (diamond) is employed to evaluate the radiative intensity in the middle of the control volume knowing the radiative intensities on the control volume boundaries [35]. For a number of control volumes larger than 190, the numerical results were found to be independent of the number of control volumes [18], i.e., numerical convergence was reached.

C. Transmitted and Reflected Intensity Calculations

The intensities leaving the sample with smooth interfaces can be written as [18]

$$I_\lambda(0,\eta) = r_{12}\delta_{\mu_0,-\eta} I_\lambda(0,-\eta) + \left(\frac{1}{m_\lambda}\right)^2 (1-r_{12}) I_\lambda(0,\mu) \qquad \eta<0, \mu<0 \tag{27}$$

$$I_\lambda(e,\eta) = \left(\frac{1}{m_\lambda}\right)^2 (1-r_{21}) I_\lambda(e,\mu) \qquad \eta>0, \mu>0 \tag{28}$$

where the direction $\cos\eta = \cos\alpha$ with α is the measurement angle whereas $\mu = \cos\theta$ is related to η through Eq. (26).

In general, the measurement angle α is different from one of the quadrature angles θ_i selected for the numerical calculations due to refraction at the interfaces of the slab except for the direct transmission and backscattering directions (i.e., for $\eta = \pm 1$). To circumvent this difficulty, an interpolation can be used to evaluate the intensity in the measurement angle α using the computed intensity in the quadrature directions [18]. Different interpolation laws such as linear law (LL), exponential law (EL) and combined exponential-linear law (ELL) can be used.

D. Adaptive Composite Quadrature

Another way of avoiding the difficulty related to interpolation is to use an adaptive composite quadrature (ACQ) [37] to solve Eq. (20). In the present study, the ACQ quadrature depends on the radiation wavelength and consists of Mb/2 directions in each hemisphere such that Mb > Nb (Fig. 3). Here also, Mb must be a positive even number.

In the forward hemisphere, the first Nb/2 directions among the Mb/2 directions are related directly to the experimental direction through Snell's law. Rearranging Eq. (26) yields

$$\mu_i = \cos\{\sin^{-1}[m_\lambda^{-1}\sin(\cos^{-1}\eta_i)]\} \qquad \text{for } i=1 \text{ to Nb}/2 \tag{29}$$

The weight w_i associated to direction i from 1 to Nb/2 can be geometrically interpreted as the solid angle $\Delta\Omega_i$ around each direction divided by 2π, i.e.,

$$w_i = \frac{\Delta\Omega_i}{2\pi} = \int_{\theta_{i,\min}}^{\theta_{i,\max}} \sin\theta\,\mathrm{d}\theta = -\int_{\mu_{i,\min}}^{\mu_{i,\max}} \mathrm{d}\mu = \mu_{i,\min} - \mu_{i,\max} \qquad \text{for } i=1 \text{ to Nb}/2 \tag{30}$$

where $\theta_{i,\min}$ and $\theta_{i,\max}$ are the minimum and maximum polar angles around direction i, respectively. For $i=1$, $\mu_{1,\min}=1$ and $\mu_{1,\max} = \cos\{\sin^{-1}[m_\lambda^{-1}\sin(\cos^{-1}\eta_{1,\max})]\}$ with $\eta_{1,\max} = 1-\Delta\Omega_0/2\pi$. For i from 2 to Nb/2, $\mu_{i,\min} = \mu_{i-1,\max}$ and $\mu_{i,\max} = \cos\{\sin^{-1}[m_\lambda^{-1}\sin(\cos^{-1}\eta_{i,\max})]\}$ with $\eta_{i,\max} = \eta_{i-1,\max} - w_i'$. Here w' refers to the angular weight of the two Gaussian quadratures associated to the experimental direction i.

Because of the refraction mismatch between the sample and the surrounding medium, these Nb/2 directions are confined under a critical angle defined by

$$\mu_{\mathrm{Nb}/2,\max} = \cos[\sin^{-1}(1/m_\lambda)] \tag{31}$$

Then, the Mb/2-Nb/2 remaining directions between $\mu_{\mathrm{Nb}/2,\max}$ and $\mu_{\mathrm{Nb}/2}=0$ can be defined by using the standard quadrature rules. However, because the intensity variation outside the critical angle is quasilinear, a regular discretization is sufficient.

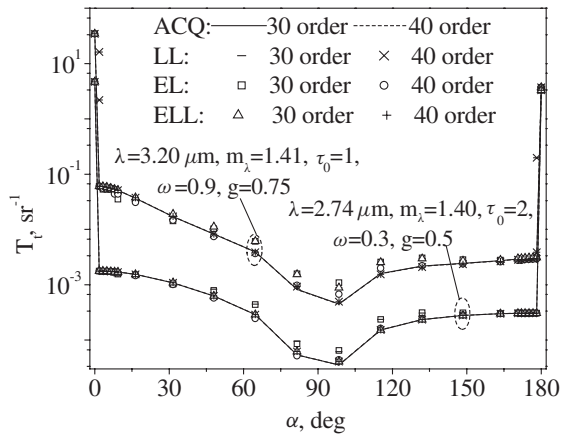

a)

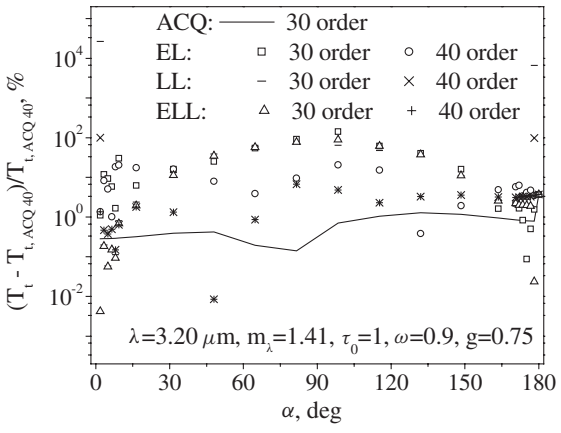

b)

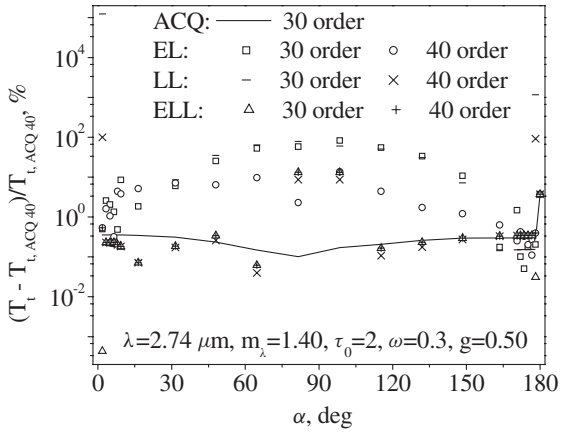

c)

Fig. 5 a) Comparison between transmittances from the interpolation laws (LL, EL, and ELL) and the ACQ; b) relative transmittance deviation of the different interpolation laws (LL, EL, and ELL) compared with the ACQ for $\lambda = 3.20\ \mu$m; c) relative transmittance deviation of the different interpolation laws (LL, EL, and ELL) compared with the ACQ for $\lambda = 2.74\ \mu$m.

Therefore, the remaining direction cosines can be expressed as

$$\begin{cases} \mu_{\mathrm{Nb}/2+1} = \cos(\theta_{\mathrm{Nb}/2,\max} + \Delta\theta/2) \\ \mu_i = \cos(\theta_{i-1} + \Delta\theta) \end{cases} \quad \text{for } i = \mathrm{Nb}/2+2 \text{ to } \mathrm{Mb}/2 \tag{32}$$

with $\Delta\theta = (\pi - 2\theta_{\mathrm{Nb}/2,\max})/(\mathrm{Mb} - \mathrm{Nb})$. The associated weights are given by

$$w_i = \cos(\theta_i - \Delta\theta) - \cos(\theta_i + \Delta\theta) \quad \text{for } i = \mathrm{Nb}/2+1 \text{ to } \mathrm{Mb}/2 \tag{33}$$

The $\mathrm{Mb}/2$ directions in the backward hemisphere and those in the forward hemisphere are symmetrical with respect to sample surface, i.e.,

$$\begin{cases} \mu_i = -\mu_j \\ w_i = w_j \end{cases} \quad \text{for } i = 1 \text{ to } \mathrm{Mb}/2 \text{ and } j = \mathrm{Mb}/2+1 \text{ to Mb} \tag{34}$$

The theoretical bidirectional transmittance obtained by using the interpolation methods with a Gaussian quadrature and the ACQ are compared. The quadrature order considered are $\mathrm{Mb} = 30$ and 40. Two cases of refracting, absorbing, and scattering but nonemitting medium assuming the HG phase function are considered: 1) $m_\lambda = 1.41$, $\beta e = \tau_0 = 1$, $\omega = 0.9$, and $g = 0.75$; and 2) $m_\lambda = 1.40$, $\beta e = \tau_0 = 2$, $\omega = 0.3$, and $g = 0.5$.

Figure 5a shows the computed transmittances in the experimental directions using three different interpolation laws, namely linear, exponential, and combined exponential-linear laws, and the ACQ for quadrature orders 30 and 40. Figures 5b and 5c depict the relative differences in directional transmittance obtained for each interpolation law with respect to the ACQ quadrature order 40. One can note that the same conclusions can be drawn for the two media considered. When the added directions (Mb-Nb) in the ACQ exceed six, corresponding to $\mathrm{Mb} = 30$, the solution of the RTE converges numerically, i.e., it is independent of the number of directions and control volumes, the relative difference in transmittance falls below 1%. The linear interpolation with quadrature order $\mathrm{Mb} = 30$ overestimates significantly the intensities near the incident direction, the error exceeds 1000% and decreases to 100% for a quadrature order $\mathrm{Mb} = 40$. The exponential interpolation with quadrature order $\mathrm{Mb} = 30$ gives errors reaching 100% in directions far either from the incident direction or from the backward direction. These errors decrease to 20% for quadrature order $\mathrm{Mb} = 40$. The combined exponential-linear law gives better results. The maximum deviation appears only in the directions around 90 deg and does not exceed 10% for quadrature order $\mathrm{Mb} = 40$. The results for each interpolation laws can be improved by increasing the quadrature order but this approach increases the CPU time and is not convenient for the inverse method. Thus, the ACQ quadrature order $\mathrm{Mb} = 30$ is adopted in the present study.

V. Results

A. Sample Characteristics

Three samples of different thickness ($e = 5$, 6, and 9.9 mm) are studied; all of them feature an average void fraction of 4% and an average bubble radius a equal to 0.64 mm. As one can see in Fig. 1, the bubbles are spherical in shape and randomly distributed. The sample thickness e and the fused quartz refractive index m_λ are used as input data in the identification process. Different correlations for m_λ have been suggested in the literature for different spectral regions [38–41]. The most widely accepted is the Malitson's correlation, which is valid over the spectral range from 0.21 to 3.71 μm at 20°C:

$$m_\lambda^2 = 1 + \frac{0.696\lambda^2}{\lambda^2 - (0.068)^2} + \frac{0.408\lambda^2}{\lambda^2 - (0.116)^2} + \frac{0.897\lambda^2}{\lambda^2 - (9.896)^2} \tag{35}$$

The validity of Eq. (35) was also confirmed by Tan [41] up to 6.7 μm. Therefore, due to its wide range of validity at room temperature, Eq. (35) is used in the present study. The identification of parameter has been performed for more than 100 different wavelengths in the spectral region from 1.67 to 4.04 μm.

B. Sensitivity Coefficients

To investigate the influence of each measurement direction on the inverse method, the sensitivity coefficients of the theoretical model based on the TPF phase function [Eq. (14)] are investigated. For illustration purposes, we consider three cases of semitransparent media with Fresnel interfaces characterized by 1) for $\lambda = 1.89$ μm, $m_\lambda = 1.44$, $\beta e = \tau_0 = 0.5$, $\omega = 0.90$, $f_1 = 0.22$, $g_1 = 0.98$, and $g_2 = 0.50$; 2) for $\lambda = 3.20$ μm, $m_\lambda = 1.40$, $\beta e = \tau_0 = 1.0$, $\omega = 0.70$, $f_1 = 0.21$, $g_1 = 0.98$, and $g_2 = 0.45$; and 3) for $\lambda = 3.96$ μm, $m_\lambda = 1.39$, $\beta e = \tau_0 = 2.5$, $\omega = 0.35$, $f_1 = 0.17$, $g_1 = 0.96$, and $g_2 = 0.35$. The variations of the absolute dimensionless sensitivity coefficients defined as $\Pi = p_l/T_{ei}(\partial T_{ti}/\partial p_l)$ for $l = \beta$, ω, f_1, g_1, and g_2 and $i = 1$ to Nb, are depicted in Figs. 6a–6c versus the measurement angle α. The sensitivity of the theoretical bidirectional transmittance and reflectance to β increases when the optical thickness increases particularly in the incident direction. The sensitivity to ω tends to 0 near the incident direction and increases with the measurement angle. This sensitivity decreases slightly as the optical thickness increases but remains significant and close to unity. For optically thin medium, the sensitivity to ω has similar trend to those of β. As far as the parameter f_1 is concerned, the model is sensitive only to directions near the forward and backward directions. The parameter g_2 has the lowest sensitivity for optically thin medium. On the contrary, the sensitivity coefficient is the largest for the parameter g_1, especially around the forward and backward directions.

It is clear that the first direction is essential to determine the extinction coefficient of media with moderate optical thickness ($\tau_0 = 1$ and 2.5). In addition, measurements in the scattering directions are required to identify ω and β for $\tau_0 = 0.5$. In the case of optically thin media ($\tau_0 < 1$), ω and β may be linearly dependent resulting in a high condition number, i.e., an ill-conditioned system, such that their simultaneous estimation appears difficult. Some directions near the forward ($i = 2$–5) and backward directions ($i = $ Nb-4 to Nb) are certainly sufficient to determine the parameters f_1 and g_1. Finally, the computation of the parameter g_2 requires measurements in the scattering directions.

C. Influence of the Number of Measurements and the Experimental Uncertainties

To investigate the influence of the number of measurements on the parameter identification, a parametric study was performed by considering different combinations of forward and backward measurements such as 12/12, 12/5, 7/12, 9/7, and 9/9. The first number refers to the number of forward measurements counted from the incident direction ($\eta = \mu_0 = 1$) and the second one corresponds to the number of backward measurements counted from the specular direction ($\eta = -1$). The relaxation factor γ used in Eq. (5) is chosen equal to 0.5. Instead of using experimental measurements where the exact solutions are unknown, we used simulated measurements based on the solutions of Eq. (20) by using the TPF model and the radiative characteristics obtained from the identification results (Section V.G): 1) for $\lambda = 1.89$ μm, $m_\lambda = 1.44$, $\beta e = \tau_0 = 0.5$, $\omega = 0.90$, $f_1 = 0.22$, $g_1 = 0.98$, and $g_2 = 0.50$; 2) for $\lambda = 3.20$ μm, $m_\lambda = 1.40$, $\beta e = \tau_0 = 1.0$, $\omega = 0.70$, $f_1 = 0.21$, $g_1 = 0.98$, and $g_2 = 0.45$; and 3) for $\lambda = 3.96$ μm, $m_\lambda = 1.39$, $\beta e = \tau_0 = 2.5$, $\omega = 0.35$, $f_1 = 0.17$, $g_1 = 0.96$, and $g_2 = 0.35$. To take into account the experimental uncertainties, the simulated measurements (T_t) are corrupted by adding normally distributed random errors [42]

$$T_{et} = T_{tt} + \xi\sigma_i \qquad \text{for } i = 1 \text{ to Nb} \tag{36}$$

where $0 < \xi < 1$ is a normally distributed random number and σ_i is the standard deviation for an experimental error χ_i corresponding to a confidence interval of 99%. The standard deviation σ_i for direction i

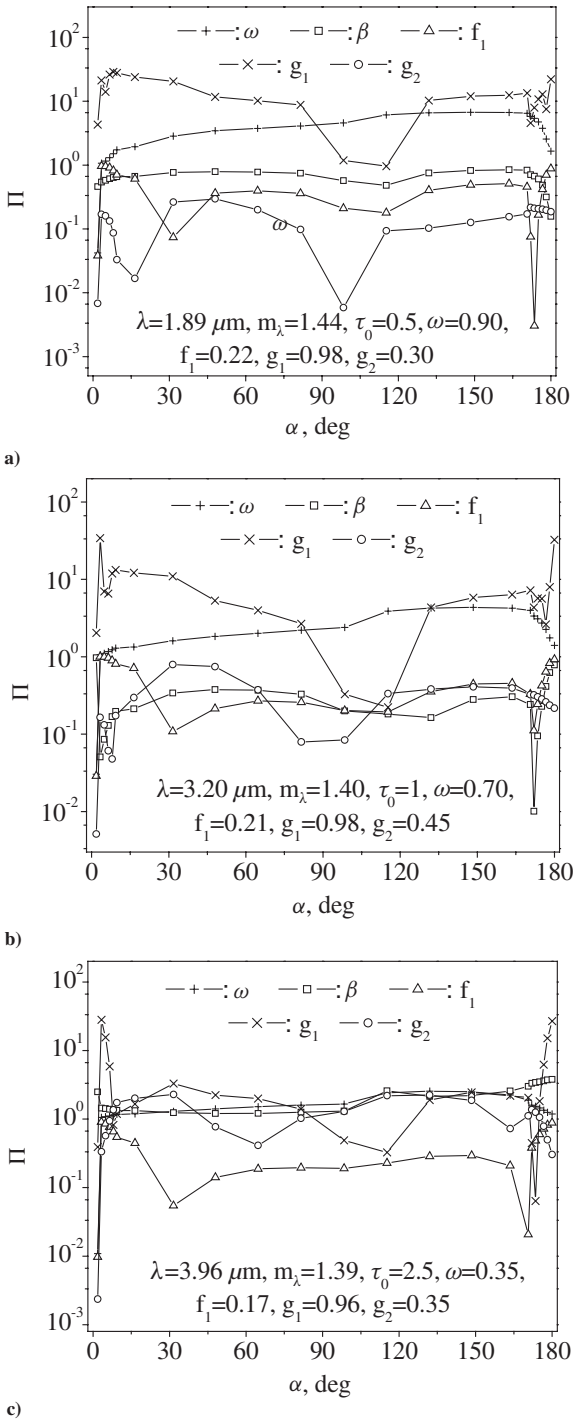

Fig. 6 Dimensionless sensitivity coefficients for a) $\lambda = 1.89\ \mu$m, b) $\lambda = 3.20\ \mu$m, and c)$\lambda = 3.96\ \mu$m.

is expressed as

$$\sigma_i = \frac{\chi_i \bar{T}_i}{2.58} \tag{37}$$

where $\bar{T}_i$ is the average transmittance defined as

$$\begin{cases} \bar{T}_i = T_{ti} & \text{for } i = 1, 2, \text{Nb}-1, \text{ and Nb} \\ \bar{T}_i = \frac{1}{(\text{Nb}/2-3)+1} \sum_{j=3}^{\text{Nb}/2} T_{tj} & \text{for } i = 3, \text{Nb}/2 \\ \bar{T}_i = \frac{1}{[\text{Nb}-2-(\text{Nb}/2+1)]+1} \sum_{\text{Nb}/2+1}^{\text{Nb}-2} T_{tj} & \text{for } i = \text{Nb}/2+1, \text{Nb}-2 \end{cases} \tag{38}$$

The relative error χ_i associated with the direction i is chosen to be equal to the largest experimental error whose origins have been discussed in Section III.B. After several measurements, they are estimated as:

$$\begin{cases} \chi_1 = 10\% \\ \chi_2 = 20\% \\ \chi_i = 10\% & \text{for } i = 3, \text{Nb}-2 \\ \chi_{\text{Nb}-1} = 20\% \\ \chi_{\text{Nb}} = 40\% \end{cases} \tag{39}$$

The exact and corrupted bidirectional transmittances are shown in Figs. 7a–7c as a function of the measurement angle α. As one can see,

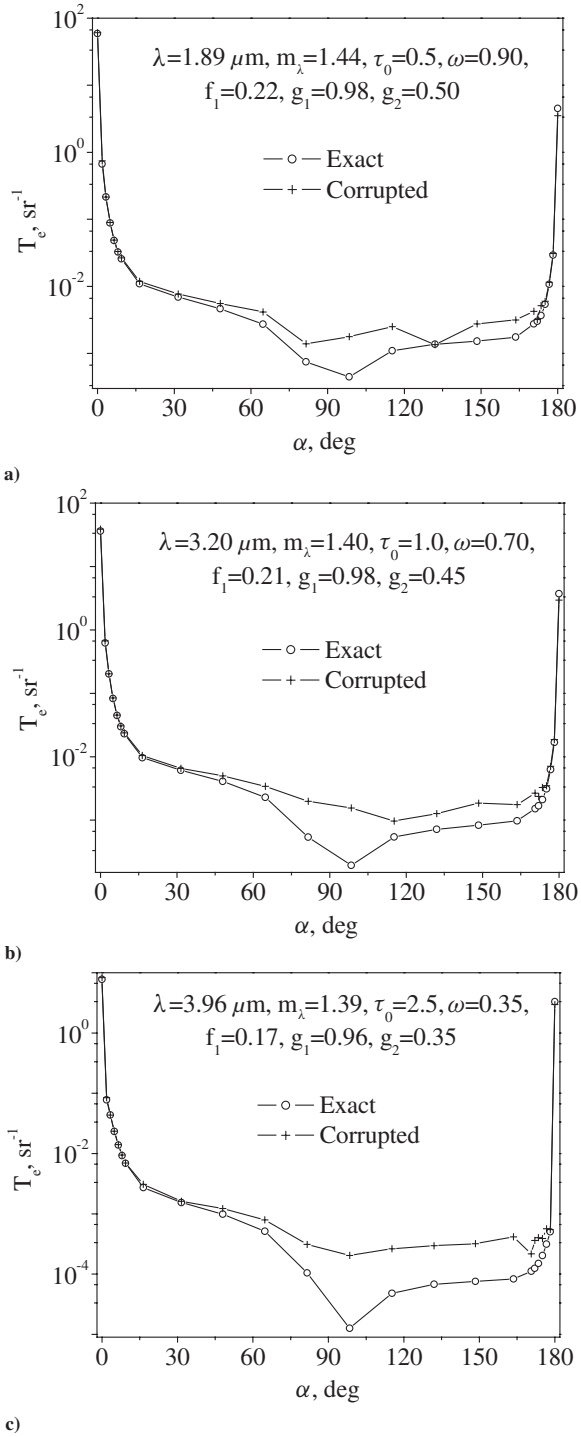

Fig. 7 Simulated exact and corrupted bidirectional transmittances for a) $\lambda = 1.89\ \mu$m, b) $\lambda = 3.20\ \mu$m, and c) $\lambda = 3.96\ \mu$m.

Table 1 Influence of bidirectional measurement number (MN) on the identified parameters from the approaches Al and A2 for $\lambda = 1.89$ μm and $m_\lambda = 1.44$, with the exact parameters $\beta_{exact} = 50$ m^{-1}, $\omega_{exact} = 0.9$, $f_{1exact} = 0.22$, $g_{1exact} = 0.98$, and $g_{2exact} = 0.5$, and the initial parameters $\beta_0 = 70$ m^{-1}, $w_0 = 0.5$, $f_{10} = 0.5$, $g_{10} = 0.7$, and $g_{20} = 0.2$.

MN	$\Delta\beta/\beta_{exact}$, %		$\Delta\omega/\omega_{exact}$, %		$\Delta f_1/f_{1exact}$, %		$\Delta g_1/g_{1exact}$, %		$\Delta g_2/g_{2exact}$, %		Iteration number (IN)		CN	
	A2	A1	A2	A1	A2	A1	A2	A1	A2	A1	A2	A1	A2	A1
12/12	4.52	13.92	−9.09	−10.41	5.12	5.56	−0.32	−0.16	−5.29	−7.72	24	15	3.1×10^7	1.1×10^3
12/5	−2.58	13.92	−7.02	−8.88	−0.47	2.48	−0.46	−0.10	−4.76	−7.27	27	15	9.3×10^7	1.2×10^3
7/12	——	13.92	-	−10.56	——	6.83	——	−0.12	——	−12.53	——	35	——	1.5×10^3
9/7	——	13.92	-	−8.32	——	4.66	——	0.07	——	0.37	——	17	——	1.4×10^3
9/9	2.12	13.92	−6.63	−8.68	3.42	7.57	−0.21	0.15	−2.44	2.38	23	70	2.2×10^7	1.0×10^3

Table 2 Influence of bidirectional MN on the identified parameters from the approaches Al and A2 for $\lambda = 3.20$ μm and $m_\lambda = 1.40$, with the exact parameters $\beta_{exact} = 100$ m^{-1}, $\omega_{exact} = 0.7$, $f_{1exact} = 0.21$, $g_{1exact} = 0.98$, and $g_{2exact} = 0.45$, and the initial parameters $\beta_0 = 70$ m^{-1}, $w_0 = 0.5$, $f_{10} = 0.5$, $g_{10} = 0.7$, and $g_{20} = 0.2$.

MN	$\Delta\beta/\beta_{exact}$, %		$\Delta\omega/\omega_{exact}$, %		$\Delta f_1/f_{1exact}$, %		$\Delta g_1/g_{1exact}$, %		$\Delta g_2/g_{2exact}$, %		IN		CN	
	A2	A1	A2	A1	A2	A1	A2	A1	A2	A1	A2	A1	A2	A1
12/12	1.47	1.98	−13.78	−13.80	21.83	22.19	0.27	0.29	22.32	22.38	25	16	7.3×10^6	7.2×10^2
12/5	−132.89	1.98	−30.15	−13.24	−61.10	19.51	−1.50	0.22	−7.23	21.24	31	20	2.8×10^{11}	1.0×10^3
7/12	1.41	——	−16.45	——	21.14	——	0.10	——	−0.75	——	34	——	1.1×10^7	——
9/7	2.61	1.98	−10.57	−10.67	14.92	14.59	0.25	0.20	14.76	14.48	21	16	7.4×10^6	9.5×10^2
9/9	2.19	1.98	−11.92	−11.91	19.14	19.21	0.36	0.35	19.04	19.01	24	14	5.9×10^6	8.0×10^2

Table 3 Influence of bidirectional measurement number on the identified parameters from the approaches Al and A2 for $\lambda = 3.96$ μm and $m_\lambda = 1.39$, with the exact parameters $\beta_{exact} = 250$ m^{-1}, $\omega_{exact} = 0.35$, $f_{1exact} = 0.17$, $g_{1exact} = 0.96$, and $g_{2exact} = 0.35$, and the initial parameters $\beta_0 = 70$ m^{-1}, $w_0 = 0.5$, $f_{10} = 0.5$, $g_{10} = 0.7$, and $g_{20} = 0.2$, Nb = 24.

MN	$\Delta\beta/\beta_{exact}$, %		$\Delta\omega/\omega_{exact}$, %		$\Delta f_1/f_{1exact}$, %		$\Delta g_1/g_{1exact}$, %		$\Delta g_2/g_{2exact}$, %		IN		CN	
	A2	A1	A2	A1	A2	A1	A2	A1	A2	A1	A2	A1	A2	A1
12/12	1.21	1.27	−35.41	−35.33	40.25	40.23	−0.30	−0.26	59.60	59.62	24	14	1.8×10^6	1.6×10^2
12/5	−318.91	1.27	−149.57	−32.84	−206.36	36.32	−3.93	−0.36	−75.51	50.59	31	15	2.8×10^{13}	1.8×10^2
7/12	1.10	1.27	−39.78	58.47	39.50	−102.13	−0.41	−0.46	37.63	−171.85	26	15	1.6×10^6	2.5×10^5
9/7	1.40	1.27	−31.94	−32.18	39.18	39.01	−0.14	−0.11	68.78	68.64	38	15	2.0×10^6	4.4×10^2
9/9	1.45	1.27	−31.77	−32.04	38.90	38.75	−0.15	−0.12	68.07	68.06	24	15	2.0×10^6	4.3×10^2

the largest absolute errors correspond to the directions far from the direction of the incident radiation.

Moreover, two identification approaches are tested: approach A1 consists of direct computation of β from Eq. (18) and simultaneous estimation of ω, f_1, g_1, and g_2 parameters; approach A2 consists of estimating simultaneously β, ω, f_1, g_1, and g_2. The initial values of these parameters are taken identical in both cases. The difference between the identified parameters and the exact solutions, the number of iterations and the condition number are summarized in Tables 1–3. The following conclusions can be drawn:

1) The parameters ω, f_1, and g_2 are the most sensitive to the experimental uncertainties. Their deviations from the exact solutions increase as the optical thickness increases. On the contrary, the parameter g_1 is not influenced by the experimental uncertainty and is in good agreement with the exact solution (the deviation is less than 4% in all cases).

2) When an insufficient number of measurements is used such as 12/5, 7/12, and/or 9/7, either the inverse process does not converge or it converges toward a wrong solution (the errors can reach 300%). However, if too many noisy measurements are used, such as 12/12, the computation leads to large errors that may reach up to 20% and 60% depending on the optical thickness. In our case, the 9/9 combination gives a good compromise between convergence and accuracy for every wavelength, and will be used in the identification using experimental data.

3) The condition number obtained by simultaneous estimation of all parameters (approach A2), is very large (10^{+6} to 10^{+13}) for all the optical thicknesses studied. When the CN is greater than 10^{+10}, the inversion procedure converges toward erroneous solutions. On the other hand, the independent computation of the extinction coefficient (approach A1) leads to an acceptable condition number ($\sim 10^{+3}$).

4) The directly computed extinction coefficient (approach A1) is less precise than that retrieved from the approach A2 for small optical thickness ($\tau_0 = 0.5$). This deviation is due to the approximation of the intensity variation as a third order polynomial function.

D. Influence of the Parameters' Initial Values

The parameter identification is performed by using the simulated experimental transmittance and reflectance described in Section V.C with nine forward and nine backward measurements. To investigate the effect of the parameters' initial value on the identification results, three combinations of initial parameters are considered as reported in Tables 4–6. In addition, the two identification approaches A1 and A2 are compared. The relative difference between the computed and exact parameters, the number of iterations, and the condition number are summarized in Tables 4–6. One can note that the initial guesses for the unknown parameters do not affect the results of approach A1 but only the number of iterations, i.e., the CPU time. However, the approach A2 is influenced by the parameters' initial values especially for absorbing materials ($\tau_0 = 2.5$). Therefore, approach A1 is more stable than A2 with respect to the initial guesses for the radiation characteristics to be identified.

E. The Two-Step Inverse Process

The analysis in Sections V.C and V.D show that nine forward and nine backward measurements are sufficient for the current identification of parameter. The approach A1 using the direct computation of β is more robust than the simultaneous parameter estimation (approach A2). It avoids dealing with a very ill-conditioned system, which reduces the efficiency of the method. However, it is less precise for small optical thickness. The approach A2 is always

Table 4 Influence of the parameters' initial values (piv) on the identification results from the approaches A1 and A2 for $\lambda = 1.89$ μm and $m_\lambda = 1.44$ with nine forward and nine backward measurements and the exact parameters $\beta_{exact} = 50$ m^{-1}, $\omega_{exact} = 0.90$, $f_{1exact} = 0.22$, $g_{1exact} = 0.98$, and $g_{2exact} = 0.5$. The initial parameters are piv 1: $\beta_0 = 70$ m^{-1}, $w_0 = 0.5$, $f_{10} = 0.5$, $g_{10} = 0.7$, and $g_{20} = 0.2$; piv 2: $\beta_0 = 500$ m^{-1}, $w_0 = 0.1$, $f_{10} = 0.8$, $g_{10} = 0.2$, and $g_{20} = 0.1$; and piv 3: $\beta_0 = 100$ m^{-1}, $w_0 = 0.8$, $f_{10} = 0.1$, $g_{10} = 0.7$, and $g_{20} = 0.2$.

piv	$\Delta\beta/\beta_{exact}$, %		$\Delta\omega/\omega_{exact}$, %		$\Delta f_1/f_{1exact}$, %		$\Delta g_1/g_{1exact}$, %		$\Delta g_2/g_{2exact}$, %		IN		CN	
	A2	A1	A2	A1	A2	A1	A2	A1	A2	A1	A2	A1	A2	A1
1	2.1	13.92	−6.63	−8.32	3.42	4.66	−0.21	0.07	−2.44	0.37	23	17	2.2×10^7	1.4×10^3
2	1.22	13.92	−7.47	−8.32	7.80	4.65	−0.04	0.07	4.42	0.37	62	32	1.2×10^7	1.1×10^3
3	1.18	13.92	−7.47	−8.30	7.78	4.73	−0.04	0.07	4.40	0.49	25	15	1.2×10^7	1.2×10^3

Table 5 Influence of the parameters' initial values on the identification results from the approaches A1 and A2 for $\lambda = 3.20$ μm and $m_\lambda = 1.41$, with nine forward and nine backward measurements and the exact parameters $\beta_{exact} = 100$ m^{-1}, $\omega_{exact} = 0.7$, $f_{1exact} = 0.21$, $g_{1exact} = 0.98$, and $g_{2exact} = 0.45$. The initial parameters are piv 1: $\beta_0 = 70$ m^{-1}, $w_0 = 0.5$, $f_{10} = 0.5$, $g_{10} = 0.7$, and $g_{20} = 0.2$; piv 2: $\beta_0 = 500$ m^{-1}, $w_0 = 0.1$, $f_{10} = 0.8$, $g_{10} = 0.2$, and $g_{20} = 0.1$; and piv 3: $\beta_0 = 100$ m^{-1}, $w_0 = 0.8$, $f_{10} = 0.1$, $g_{10} = 0.7$, and $g_{20} = 0.2$.

piv	$\Delta\beta/\beta_{exact}$, %		$\Delta\omega/\omega_{exact}$, %		$\Delta f_1/f_{1exact}$, %		$\Delta g_1/g_{1exact}$, %		$\Delta g_2/g_{2exact}$, %		IN		CN	
	A2	A1	A2	A1	A2	A1	A2	A1	A2	A1	A2	A1	A2	A1
1	2.19	1.98	−11.92	−10.67	19.14	14.59	0.36	0.20	19.04	14.48	24	16	5.9×10^6	9.4×10^2
2	0.04	1.52	−15.06	−15.46	10.88	15.75	−0.19	−0.01	12.95	17.00	50	25	3.3×10^7	1.4×10^3
3	−0.04	1.52	−15.10	−15.46	10.76	15.81	−0.20	0.00	12.86	16.99	37	16	3.7×10^7	1.4×10^3

Table 6 Influence of the parameters' initial values on the identification results from the approaches A1 and A2 for $\lambda = 3.96$ μm and $m_\lambda = 1.39$, with nine forward and nine backward measurements and the exact parameters $\beta_{exact} = 250$ m^{-1}, $\omega_{exact} = 0.35$, $f_{1exact} = 0.17$, $g_{1exact} = 0.96$, and $g_{2exact} = 0.35$. The initial parameters are piv 1: $\beta_0 = 70$ m^{-1}, $w_0 = 0.5$, $f_{10} = 0.5$, $g_{10} = 0.7$, and $g_{20} = 0.2$; piv 2: $\beta_0 = 500$ m^{-1}, $w_0 = 0.1$, $f_{10} = 0.8$, $g_{10} = 0.2$, and $g_{20} = 0.1$; and piv 3: $\beta_0 = 100$ m^{-1}, $w_0 = 0.8$, $f_{10} = 0.1$, $g_{10} = 0.7$, and $g_{20} = 0.2$.

piv	$\Delta\beta/\beta_{exact}$, %		$\Delta\omega/\omega_{exact}$, %		$\Delta f_1/f_{1exact}$, %		$\Delta g_1/g_{1exact}$, %		$\Delta g_2/g_{2exact}$, %		IN		CN	
	A2	A1	A2	A1	A2	A1	A2	A1	A2	A1	A2	A1	A2	A1
1	2.19	1.98	−11.92	−10.67	19.14	14.59	0.36	0.20	19.04	14.48	24	16	5.9×10^6	9.4×10^2
2	0.04	1.52	−15.06	−15.46	10.88	15.75	−0.19	−0.01	12.95	17.00	50	25	3.3×10^7	1.4×10^3
3	−0.04	1.52	−15.10	−15.46	10.76	15.81	−0.20	0.00	12.86	16.99	37	16	3.7×10^7	1.4×10^3

Table 7 Influence of the phase function model on the radiative characteristics for 6 mm sample thickness at different wavelengths.

λ, μm	k_{bulk}, m^{-1}	β_{HG}, m^{-1}	β_{TPF}, m^{-1}	ω_{HG}	ω_{TPF}	k_{HG}, m^{-1}	k_{TPF}, m^{-1}	g_{HG}	g_{TPF}
1.89	5.94	75.2	78.23	0.47	0.94	39.85	4.06	0.95	0.70
2.76	151.61	170.74	176.48	0.17	0.27	141.71	128.28	0.93	0.84
3.96	204.04	262.21	264.18	0.14	0.23	225.50	201.97	0.94	0.81

characterized by a large CN and requires a better knowledge of the initial parameters.

Moreover, one can note that these two identification schemes are complementary. Thus, this suggests performing two successive inversion procedures to optimize the final results. First, a preliminary calculation using approach A1 is carried out which provides an approximate value of the unknown parameters. Then, a second identification step based on approach A2 is performed using the results from approach A1 as initial guesses. This second step can be done without estimating g_1 because it can be determined precisely from the first step (see Section V.D). By using this two-step inverse procedure, there are no restrictions either on the parameters' initial value or on the optical thickness range. This two-step inversion scheme is applied in the current study.

F. Influence of the Phase Function Model

To investigate the effects of the scattering phase function model, the radiative parameters are identified by using measurements corresponding to the 6 mm thick sample. The two phase function models considered are the HG and the TPF. The identified parameters are summarized in Table 7 for typical wavelengths. The absorption coefficient of the fused quartz $k_{bulk} = 4\pi\kappa_{bulk}/\lambda$ is also reported on the same table where the absorption index κ_{bulk} is taken from Dombrovsky et al. [23] The resulting bidirectional transmittances are shown in Figs. 8a and 8b.

Table 7 indicates that the phase function model has significant influence on the retrieved radiative characteristics, especially in the spectral region where fused quartz is transparent (from 1.67 to 2.7 μm and 2.9 to 3.5 μm in this study but the case for $\lambda = 1.89$ μm is presented in Table 7). As for the bidirectional transmittance and reflectance reported in Fig. 8, one can note that the theoretical results obtained using the TPF function gives good agreement with the measured bidirectional transmittance and reflectance whereas results from the HG function agree only for the five forward ($i = 1$ to 5) and three backward directions ($i =$ Nb-4 to Nb-1). Overall, the HG function fails to properly describe the directional scattering behavior of the studied material.

G. Identified Radiative Characteristics

The radiative characteristics (Figs. 9a–9f) are determined from the three samples of different thickness previously described. For comparison, the bulk quartz radiative characteristic and the average results obtained by Baillis et al. [18] using the HG phase function are also reported.

First, one can conclude that the retrieved parameters are independent of samples thickness. The observed dispersion of data is

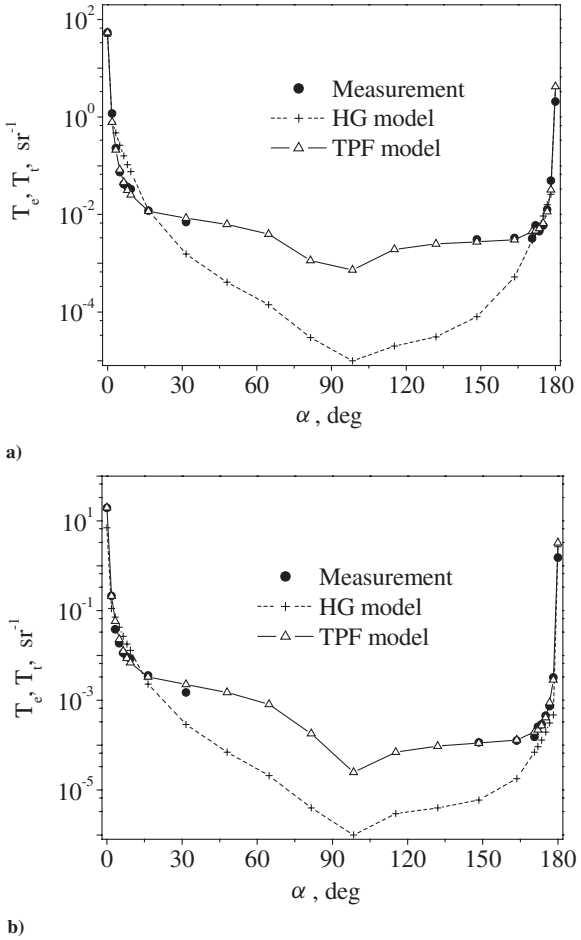

Fig. 8 Influences of the phase function model on the transmittances for the sample $e = 6$ mm a) at $\lambda = 1.89$ μm and b) at $\lambda = 3.96$ μm.

mainly attributed to the measurement uncertainties. The standard deviation is especially large for the parameter g_2 reaching about 12%.

Overall, the retrieved radiation characteristics tend to disagree with previously reported data [18] except for the extinction coefficient which can be estimated properly using the HG function. This is mainly due to the phase function model adopted in the theoretical formulations because it was shown to have little effect on the extinction coefficient but a significant one on the absorption and scattering coefficients (see Sec. V.F). However, in all cases, results using the HG model gives a small scattering albedo associated with a highly forward anisotropic phase function and an absorption coefficient 8–10 times higher than that of bulk quartz (k_{bulk}). On the contrary, the retrieved absorption coefficient using the TPF model is of the same order of magnitude as that of bulk quartz.

Moreover, the scattering behavior of the porous quartz is generally forward anisotropic with g about 0.78, its absorption coefficient is slightly smaller than that of the bulk material, and the scattering dominates the extinction ($\omega \sim 0.8$–0.9) in the transparency bands of fused quartz. This means that the bubbles are nonabsorbing but only scatter radiation and the quartz matrix is the only absorbing substance.

H. Comparison with Hemispherical Measurements and Influences of Experimental Uncertainties

To verify that the retrieved parameters represent accurately the radiative characteristics of the material studied, the calculated hemispherical transmittance termed T_t^+ and reflectance termed T_t^- based on 1) the current identified parameters and 2) the results of Baillis et al. [18] are compared with those measured experimentally and denoted T_e^+ and T_e^-. The Fourier–Transform InfraRed spectrometer is used in combination with a gold-coated integrating sphere (CSTM RSA-DI-40D) to measure the spectral hemispherical transmittance T_e^+ and reflectance T_e^-. The experimental errors are evaluated for each sample from five different measurements. Depending on the wavelength, errors range from 3 to 8% for transmittance and from 9 to 16% for reflectance. The average radiative

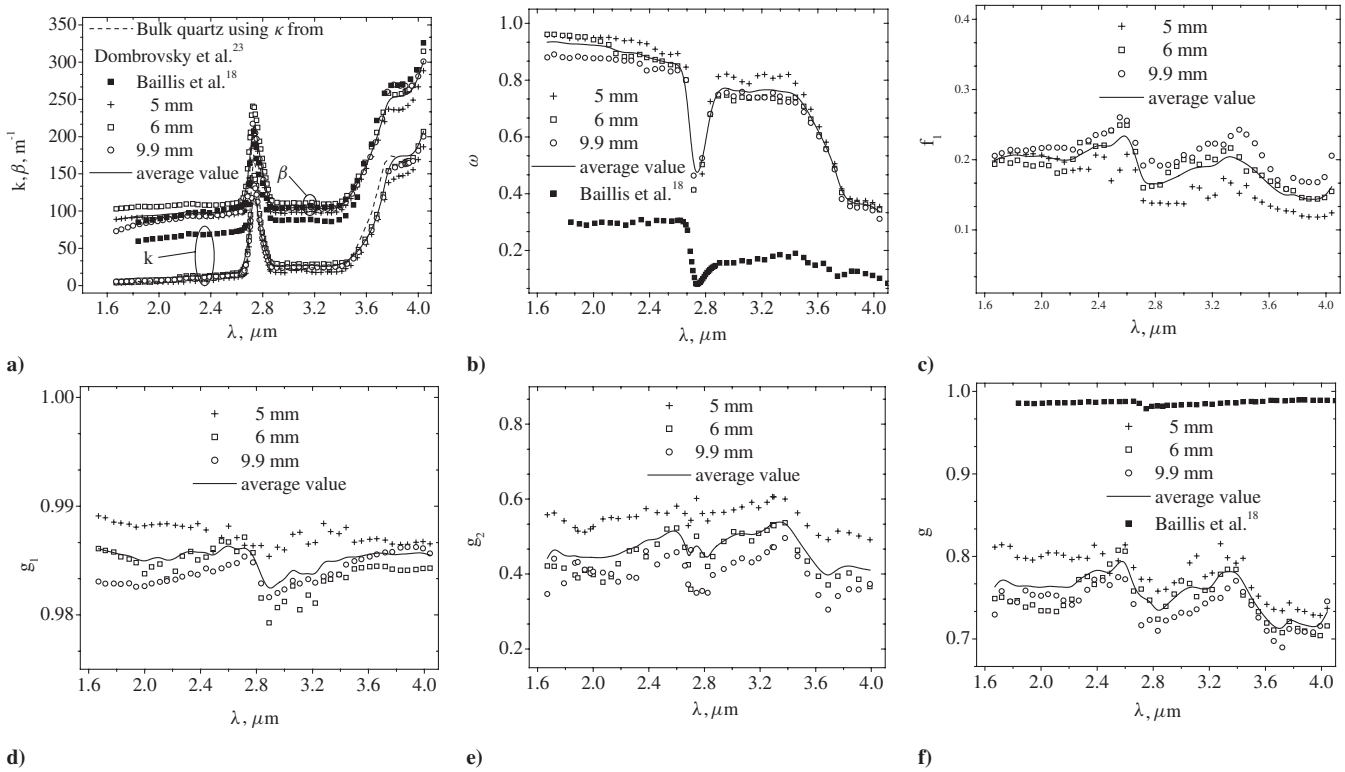

Fig. 9 a) Identified extinction (β) and absorption (k) coefficients, b) identified scattering albedo ω, c) identified scattering parameter f_1, d) identified scattering parameter g_1, e) identified scattering parameter g_2, and f) corresponding asymmetry factor $\langle g \rangle$.

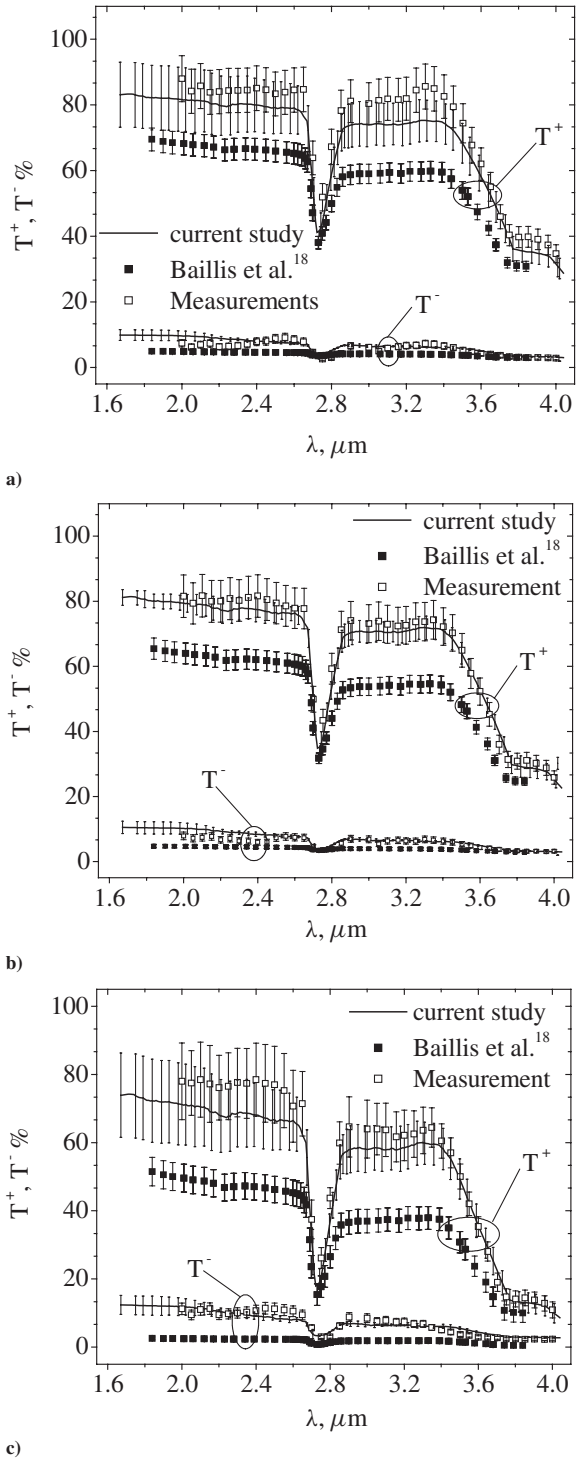

Fig. 10 Comparison between the computed and measured hemispherical transmittance and reflectance for the samples a) $e = 5$ mm, b) $e = 6$ mm, and c) $e = 9.9$ mm.

characteristics are introduced in the RTE [Eq. (20)] to compute the hemispherical transmittance and reflectance (after integration of the bidirectional transmittance over each hemisphere). The computational errors are evaluated as follows: First, Eq. (20) is solved for each sample thickness by using the associated radiative parameters, then the standard deviation are determined from the computed hemispherical transmittances and reflectances of different thicknesses. The comparisons are reported in Figs. 10a–10c. Overall, good agreement is observed between the measured hemispherical transmittances and reflectances, and their values computed using the radiative characteristics retrieved with the TPF function. On the other hand, the numerical results obtained using the radiative parameters reported by Baillis et al. [18] are always smaller than the hemispherical transmittance T_e^+ and reflectance T_e^- measurements. This can be attributed to the underestimation of the scattering albedo and overestimation of the absorption coefficient obtained when the HG phase function is adopted.

Finally, the comparison of numerical results with hemispherical measurements not only enables one to quantify the experimental errors but also offers an efficient validation tool.

VI. Conclusions

Recently, the experimental determination of radiative characteristics of fused quartz containing bubbles was performed using an inverse method based on bidirectional transmittance measurements. The Henyey–Greenstein phase function was used in the theoretical model based on the RTE. Because of refraction at both interfaces of the slab, the theoretical transmittance and reflectance in the measurement directions were evaluated by using an interpolation law. In the present study, several improvements are proposed particularly for 1) the scattering phase function model, 2) the identification procedure, and 3) the quadrature used in the theoretical calculations. From the preceding discussion, the following conclusions can be drawn:

1) The importance of the phase function model on the inverse method based on bidirectional transmittance measurements has been demonstrated. The use of a common scattering phase function such as the Henyey–Greenstein function underestimates the scattering coefficient and overestimates the absorption coefficient whereas it properly estimates the extinction coefficient. The present study proposed a more elaborate phase function, the so-called truncated phase function, which depends on three parameters and enables one to take into account the complex scattering behavior of the samples. The hemispherical transmittance and reflectance computed using these newly retrieved coefficients gives better agreement with the experimental measurements than those obtained using the previously reported radiative characteristics [18].

2) The interpolation methods used to evaluate the theoretical transmittance in the measurement directions were shown to be less accurate than the proposed adaptive composite quadrature unless a high quadrature order was used. The use of an adaptive quadrature has been proposed and found to be advantageous in terms of both computational time and precision.

3) The importance of the choice of the measurement directions on the identification results has been highlighted. It is recommended to perform the sensitivity coefficients analysis for similar study using bidirectional transmittance and reflectance measurements.

4) A new inverse method based on a two-step inversion procedure is proposed. It uses a preliminary parameters estimation step. This technique enables one a) to avoid the errors induced by the direct computation of the extinction coefficient from the collimated transmittance and b) to accelerate the convergence.

5) The radiative characteristics of the porous fused quartz were then identified and shown to be independent of the sample thickness. Unlike the results obtained using the Henyey–Greenstein function, the absorption coefficient of porous samples of porosity equal to 4% obtained using the TPF phase function is slightly smaller than that of the dense matrix. Compared with the previously published data, the current radiative characteristics appear to be in better agreement with physical intuition.

6) The limitations of the experimental setup to measure the bidirectional measurements have been pointed out. In particular, the influence of the measurement number, the measurement noises, and the alignment uncertainties on the results of the inverse method have been observed. To obtain more reliable measurements, a more sensitive detector is required to improve accuracy.

7) Finally, the same experimental methodology can be used to characterize other semitransparent materials.

Acknowledgments

The authors are indebted to William Anderson and Richard Marlor of Osram Sylvania for providing the fused quartz samples.

References

[1] Viskanta, R., and Mengüç, P., "Radiative Transfer in Dispersed Media," *Applied Mechanics Reviews*, Vol. 42, No. 9, 1989, pp. 241–259.

[2] Baillis, D., and Sacadura, J. F., "Thermal Radiation Properties of Dispersed Media: Theoretical Prediction and Experimental Characterization," *Journal of Quantitative Spectroscopy & Radiative Transfer*, Vol. 67, No. 5, 2000, pp. 327–363.

[3] Glicksman, L. R., Marge, A. L., and Moreno, J. D., "Radiation Heat Transfer in Cellular Foam Insulation," *Developments in Radiative Heat Transfer*, Vol. 203, American Society of Mechanical Engineers, New York, 1992, pp. 45–54.

[4] Kuhn, J., Ebert, H. P., Arduini-Chuster, M. C., Büttner, D., and Fricke, J., "Thermal Transfer in Polystyrene and Polyurethane Foam Insulations," *International Journal of Heat and Mass Transfer*, Vol. 35, No. 7, 1992, pp. 1795–1801.

[5] Doermann, D., and Sacadura, J. F., "Heat Transfer in Open Cell Foam Insulation," *Journal of Heat Transfer*, Vol. 118, No. 1, 1996, pp. 88–93.

[6] Pilon, L., and Viskanta, R., "Apparent Radiation Characteristics of Semitransparent Media Containing Gas Bubbles," *Twelfth International Heat Transfer Conference*, Vol. 1, Elsevier SAS, Paris, 2002, pp. 645–650.

[7] Fedorov, A. G., and Viskanta, R., "Radiation Characteristics of Glass Foams," *Journal of the American Ceramic Society*, Vol. 83, No. 11, 2000, pp. 2769–2776.

[8] Dombrovsky, L. A., *Radiation Heat Transfer in Disperse Systems*, Begel House, New York, 1996.

[9] Argento, C., and Bouvard, D., "A Ray Tracing Method for Evaluating the Radiative Heat Transfer in Porous Media," *International Journal of Heat and Mass Transfer*, Vol. 39, No. 15, 1996, pp. 3175–3180.

[10] Rozenbaum, O., De Souza Meneses, D., Echegut, P., and Levitz, P., "Influence of the Texture on the Radiative Properties of Semi-transparent Materials. Comparison Between Model and Experiment," *High Temperatures—High Pressures*, Vol. 32, No. 1, 2000, pp. 61–66.

[11] Tancrez, M., and Taine, J., "Characterization of the Radiative Properties of Porous Media with Diffuse Isotropic Reflecting Interfaces," *Twelfth International Heat Transfer Conference*, Vol. 1, Elsevier SAS, Paris, 2002, pp. 627–632.

[12] Wong, B. T., and Mengüç, P., "Depolarization of Radiation by Non-Absorbing Foams," *Journal of Quantitative Spectroscopy & Radiative Transfer*, Vol. 73, Nos. 2–5, 2002, pp. 273–284.

[13] Coquard, R., and Baillis, D., "Radiative Characteristics of Opaque Spherical Particles Beds: A New Method of Prediction," *Journal of Thermophysics and Heat Transfer*, Vol. 18, No. 2, 2004, pp. 178–186.

[14] Coquard, R., and Baillis, D., "Radiative Characteristics of Beds of Semi-Transparent Spheres Containing an Absorbing and Scattering Medium," *Journal of Thermophysics and Heat Transfer*, Vol. 19, No. 2, 2005, pp. 226–234.

[15] Hale, M., and Bohn, M., "Measurement of the Radiative Transport Properties of Reticulated Alumina Foams," *American Society of Mechanical Engineers/American Solar Energy Society Joint Solar Energy Conference*, ASME, New York, 1993, pp. 507–515.

[16] Hendricks, T., and Howell, J., "Absorption/Scattering Coefficients and Scattering Phase Function in Reticulated Porous Ceramics," *Journal of Heat Transfer*, Vol. 118, No. 1, 1996, pp. 79–87.

[17] Baillis, D., and Sacadura, J. F., "Identification of Polyurethane Foam Radiative Properties - Influence of Transmittance Measurements Number," *Journal of Thermophysics and Heat Transfer*, Vol. 16, No. 2, 2002, pp. 200–206.

[18] Baillis, D., Pilon, L., Randrianalisoa, H., Gomez, R., and Viskanta, R., "Measurements of Radiation Characteristics of Fused-Quartz Containing Bubbles," *Journal of the Optical Society of America A (Optics, Image Science and Vision)*, Vol. 21, No. 1, 2004, pp. 149–159.

[19] Nicolau, V. P., Raynaud, M., and Sacadura, J. F., "Spectral Radiative Properties Identification of Fiber Insulating Materials," *International Journal of Heat and Mass Transfer*, Vol. 37, No. 1, 1994, pp. 311–324.

[20] Hespel, L., Mainguy, S., and Greffet, J. J., "Radiative Properties of Scattering and Absorbing Dense Media: Theory and Experimental Study," *Journal of Quantitative Spectroscopy & Radiative Transfer*, Vol. 77, No. 2, 2003, pp. 193–210.

[21] Take-Uchi, M., Kurosaki, Y., Kashiwagi, T., and Yamada, J., "Determination of Radiation Properties of Porous Media by Measuring Emission," *JSME International Journal*, Vol. 31, No. 3, 1988, pp. 581–585.

[22] Yamada, J., and Kurosaki, Y., "Estimation of a Radiative Property of Scattering and Absorbing Media," *International Journal of Thermophysics*, Vol. 18, No. 2, 1997, pp. 547–556.

[23] Dombrovsky, L., Randrianalisoa, J., Baillis, D., and Pilon, L., "The Use of Mie Theory for Analyzing Experimental Data to Identify Infrared Properties of Fused Quartz Containing Bubbles," *Applied Optics* Vol. 44, No. 33, 2005, pp. 7021–7031.

[24] Dombrovsky, L., "The Propagation of Infrared Radiation in a Semitransparent Liquid Containing Gas Bubbles," *High Temperature*, Vol. 42, No. 1, 2004, pp. 143–150.

[25] Beck, J. V., and Arnold, K. J., *Parameter Estimation in Engineering and Science*, Wiley, New York, 1977.

[26] Raynaud, M., "Strategy for Experimental Design and the Estimation of Parameters," *High Temperatures—High Pressures*, Vol. 31, No. 1, 1999, pp. 1–15.

[27] Chu, C.-M., and Churchill, S. W., "Representation of the Angular Distribution of Radiation Scattered by a Spherical Particle," *Journal of the Optical Society of America*, Vol. 45, No. 11, 1955, pp. 958–962.

[28] Modest, M. F., *Radiative Heat Transfer*, McGraw-Hill, New York, 1993.

[29] Bohren, C. F., and Huffman, D. R., *Absorption and Scattering of Light by Small Particles*, Wiley, New York, 1983.

[30] Sacadura, J. F., Uny, G., and Venet, A., "Models and Experiments for Radiation Parameter Estimation of Absorbing, Emitting and Anisotropically Scattering Media," *Eighth International Heat Transfer Conference*, Vol. 2, Hemisphere, Washington, D.C., 1986, pp. 565–570.

[31] Hottel, H. C., and Sarofim, A. F., *Radiative Transfer*, McGraw-Hill, New York, 1967.

[32] Beder, E. C., Bass, C. D., and Shackleford, W. L., "Transmissivity and Absorption of Fused Quartz Between 0.2 μm and 3.5 μm from Room Temperature to 1500 degree C," *Applied Optics*, Vol. 10, No. 10, 1971, pp. 2263–2268.

[33] Touloukian, Y. S., and DeWitt, D. P., *Thermal Radiative Properties: Nonmetallic Solids*, Vol. 8, Thermophysical Properties of Matter, Plenum, New York, 1972.

[34] Khashan, M. A., and Nassif, A. Y., "Dispersion of the Optical Constants of Quartz and Polymethyl Methacrylate Glasses in a Wide Spectral Range: 0.2–3 μm," *Optics Communications*, Vol. 188, Nos. 1–4, 2001, pp. 129–139.

[35] Carlson, B. G., and Lathrop, K. D., "Transport Theory: The Method of Discrete Ordinates," *Computing Methods in Reactor Physics*, Gordon and Breach, New York, 1968, pp. 167–265.

[36] Kumar, S., Majumdar, A., and Tien, C. L., "The Differential-Discrete-Ordinate Method for Solution of the Equation of Radiative Transfer," *Journal of Heat Transfer*, Vol. 112, No. 1, 1990, pp. 424–429.

[37] Liou, B.-T., and Wu, C.-Y., "Radiative Transfer in a Multi-Layer Medium with Fresnel Interfaces," *Heat and Mass Transfer*, Vol. 32, Nos. 1–2, 1996, pp. 103–107.

[38] Rodney, W. S., and Spindler, R. J., "Index of Refraction of Fused Quartz for Ultraviolet, Visible, and Infrared Wavelengths," *Journal of the Optical Society of America*, Vol. 44, No. 9, 1954, pp. 677–679.

[39] Malitson, L. H., "Interspecimen Comparison of the Refractive Index of Fused Silica," *Journal of the Optical Society of America*, Vol. 55, No. 10, 1965, pp. 1205–1209.

[40] Tan, C. Z., and Arndt, J., "Temperature Dependence of Refractive Index of Glass SiO_2 in the Infrared Wavelength Range," *Journal of Physics and Chemistry of Solids*, Vol. 61, No. 8, 2000, pp. 1315–1320.

[41] Tan, C. Z., "Determination of Refractive Index of Silica Glass for Infrared Wavelengths by IR Spectroscopy," *Journal of Non-Crystalline Solids*, Vol. 223, Nos. 1–2, 1998, pp. 158–163.

[42] Silva Neto, A. J., and Özisik, M. N., "An Inverse Problem of Simultaneous Estimation of Radiation Phase Function, Albedo and Optical Thickness," *Journal of Quantitative Spectroscopy & Radiative Transfer*, Vol. 53, No. 4, 1995, pp. 397–409.